ChemComm

Platinum-like HER Onset in GNR/MoS2 Quantum Dots Heterostructure Through Curvature-dependent Electron Density Reconfiguration

Journal:	*ChemComm*
Manuscript ID	CC-COM-07-2022-003801.R1
Article Type:	Communication

COMMUNICATION

Platinum-like HER Onset in GNR/MoS_2 Quantum Dots Heterostructure through Curvature-dependent Electron Density Reconfiguration

Received 00th January 20xx,
Accepted 00th January 20xx

DOI: 10.1039/x0xx00000x

Aruna Narayanan Nair, [a] Mohammed F Sanad, [b] Venkata S. N. Chava, [a] and Sreeprasad T. Sreenivasan *[a]

Tailoring the curvature-directed lattice strain in GNRs along with optimal surface anchoring of molybdenum disulfide (MoS_2) quantum dots (QDs) can lead to a unique heterostructure with Pt-like HER activity (onset potential -60 mV). The curvature-induced electronic charge redistribution at the curved region in graphene nanoribbons allows a facile GNR-MoS_2 interfacial charge transfer in the heterostructure, making the interfacial Sulfur (S) more active towards HER. The density functional theory (DFT) calculations confirmed electronically activated interfacial S-based catalytic centers in the curved GNR-based heterostructure leading to Pt-like HER activity.

Low-dimensional (zero- (0D), one (1D), and two-dimensional (2D)) carbon materials (LDCMs) and their heterostructures are attractive noble-metal-free electrocatalysts, especially for electrocatalytic hydrogen evolution reaction (HER).[1] Formulation of vdW heterostructures with LD materials that can synergistically form a network of heterojunctions in the structure can tailor the interface characteristics and the HER activity. Typically, the enhanced HER activity in vdW heterostructures is known to be due to unique electronic coupling, interfacial electron transfer triggered by distinct work functions, and the creation of new active sites in the heterostructure.[2] Among LDCMs, carbon nanotube (CNT)-based heterostructures are one of the highly explored materials, where CNTs, due to their superior electrical conductivity, are largely used as conductive support for the more active counterparts.[3] Despite significant efforts, the electrocatalytic activity of CNTs and their heterostructures towards HER is still significantly inferior compared to the benchmark Pt catalysts.[4]

[a] *Department of Chemistry and Biochemistry*
The University of Texas at El Paso
El Paso, Texas 79968, United States
E-mail:sreenivasan@utep.edu
[b] *Department of Environmental Sciences and Engineering*
The University of Texas at El Paso
El Paso, Texas 79968, United States
† Electronic Supplementary Information (ESI) available. See DOI: 10.1039/x0xx00000x

Compared to CNTs, unzipped CNTs or graphene nanoribbons (GNRs),[5] though relatively less explored, offer additional benefits as HER catalysts, including the presence of new edge sites and higher surface area while retaining the electronic conductivity. One of the most explored pathways to prepare GNRs is the chemical unzipping of multiwalled CNTs (MWCNTs).[6] Here, the strength of oxidizing agent will control the kinetics of the unzipping process and create fully or partially unzipped CNTs when strong or weak oxidizing agents are used. Further, it is established that the curvature in graphene matrices can create a local strain, induce rehybridization of π and σ orbitals, and affect the energy dispersions, density of states (DOS), and localized electron density distribution.[7] Hence, the surface electron distribution in flat GNR (F-GNRs) from complete unzipping and the curved GNRs (C-GNRs) from partial unzipping of the CNT will be significantly different. However, the influence of curvature on the local electric fields and charge distributions and engineering it to elicit superior activity are generally not considered in GNRs-based electrocatalysts.

Here, using MoS_2 QDs and GNRs as components, we synthesized a 0D/1D MoS_2/GNR heterostructures and demonstrated for the first time how the local variation in the electron density of GNR can help derive superior catalytic activity from the interfacial Sulfur-based active sites. We chose MoS_2 QDs as the 0D component of the heterostructures because of its reported exceptional HER activity, illustrated by its position close to Pt in the volcano plot.[8] For this, two different GNRs termed C-GNR and F-GNR were synthesized from MWCNTs using a moderate and a strong oxidizing agent under controlled reaction durations. The curvature-induced electronic density redistribution and specific anchoring of MoS_2 QDs on GNRs lead to distinct differences in catalytic behaviors between F-GNR and C-GNRs and their heterostructure catalysts. The changes in electron distribution and observed activities were explored using DFT calculations, which confirm highly active interfacial sites in the vdW heterostructures.

Unzipping of MWCNTs with a strong oxidizing agent like potassium permanganate ($KMnO_4$) produced F-GNRs, whereas unzipping using milder ammonium persulfate ($(NH_4)_2S_2O_8$) resulted in C-GNRs (See †ESI, methods section).[6, 9] The amount of functional groups introduced while unzipping the CNTs is proportional to the strength of the employed oxidizing agent.[9] Hence, we expect more functional groups in samples unzipped using $KMnO_4$. Fig. S1 a-c† shows the scanning electron microscopy (SEM) and high-resolution transmission electron microscopy (HRTEM) images of pristine MWCNTs with perfect cylindrical morphology. Fig. S2 a-c† shows the representative AFM topography and height profiles for MWCNT, F-GNR and C-GNR, respectively. The AFM topography and the height profile (~135 nm) confirmed the partial unzipping and curved nature of C-GNR. Fig. S3a† shows the Raman spectra of pristine MWCNTs and the GNRs with three characteristic Raman bands around 1350 cm^{-1} (D band), 1580 cm^{-1} (G band), and 2700 cm^{-1} (2D band). The higher I_D/I_G ratio for F-GNR indicates higher defects/degree of edge functionalization (more unzipping) in the F-GNRs (Table S1†).[9] The presence of oxygen functionalities on GNR edges leads to increased lattice spacing, as shown in the X-ray diffraction (XRD) spectra (Fig. S3b†).[10] Fourier Transform Infra-red (FTIR) analysis and X-ray photoelectron spectroscopy (XPS) indicated that GNRs mainly have carboxyl groups (-COOH) presumably at the edges after unzipping (Fig. S3c†).[6] The SEM image of F-GNRs (Fig. S4 a, b†) affirms that $KMnO_4$ completely unzips the MWCNTs leading to F-GNRs. Corresponding HRTEM images (Fig. S4 c, d†) also corroborate the sheet-like morphology of F-GNRs with a slightly increased interlayer distance, supporting the XRD results. Unzipping MWCNTs using $(NH_4)_2S_2O_8$ resulted in longitudinal cuts while partially preserving the curved morphology (Fig. S5 a-c†). Similarly, the characterization of MoS_2 QDs using Raman (Fig. S6a†), UV-Vis (Fig. S6b†), XPS (Fig. S6 c, d†), and XRD (Fig. S6e†) confirmed that the MoS_2 QDs formed are 2H phase.[11] Different microscopic and spectroscopic investigations were conducted on GNR/MoS_2 vdW heterostructures to ensure their formation, chemical identity of the components, and delineate the interfacial charge transfer through heterojunctions. Fig. 1a and Fig. 1d show the schematic of F-GNR/MoS_2 and C-GNR/MoS_2 heterostructure, respectively. As shown in the schematic, we expect the MoS_2 QDs to be present on the edges in F-GNR while at the edge and the curved center in C-GNRs. Our microscopic and spectroscopic investigations and theoretical energy-based stability calculations confirmed the proposed architecture of the heterostructure. While the MoS_2 QDs were not evident in the SEM images (Fig. 1b and 1e), the HRTEM image in Fig. 1c and 1f proved the formation of the heterostructures. The HRTEM image of F-GNR/MoS_2 (Fig. 1c) revealed that the MoS_2 QDs are primarily attached along the edges of F-GNR. On the other hand, the HRTEM of the C-GNR/MoS_2 heterostructure revealed that MoS_2 QDs are anchored both at the edges and center of the curved basal planes (Fig. 1f). The XPS analysis also validated the presence of GNR and MoS_2 QDs in the heterostructures (Fig. 1 g-j, Fig. S7 a-g†) and a potential charge transfer between the components. The comparison of high-resolution XPS scans of the S 2p region in pristine MoS_2, F-GNR/MoS_2, and C-GNR/MoS_2 vdW heterostructures revealed a shift towards lower binding energy for the S 2p peak in the heterostructure compared to pristine MoS_2 QDs, implying the potential transfer of electrons from GNRs to MoS_2 QDs (Fig. 1 h, j).[12] Such charge transfer from GNR to MoS_2 QDs in the vdW heterostructure can enhance their HER activity (as seen in the next section). The Raman spectra of vdW heterostructures (Fig. 1k) show E^1_{2g} and A_{1g} of MoS_2 QDs and the D and G bands of the GNRs, again pointing to the successful formation of GNR/MoS_2 vdW heterostructure. The corresponding blue shift of G band in the heterostructure compared to pristine GNRs also confirms the charge transfer from GNRs to MoS_2 QDs (Fig. S8†).[13]Additionally, Kelvin Probe Force Microscopy (KPFM) measurements showed no variation in the surface charges confirming that the interaction between GNR and MoS_2 is purely via van der Waals force (Fig. S9†).

After characterizing the GNR/MoS_2 vdW heterostructures, we studied their electrocatalytic HER performance. First, the HER activities of pristine GNRs (i.e., F-GNRs and C-GNRs) and MoS_2 QDs were explored (Fig. S10†). The C-GNR exhibited an onset potential of -0.510 V vs. RHE and an overpotential of -0.585 V vs. RHE (at j = 20 mA/cm^2), whereas F-GNR displayed a higher onset potential of -0.534 V vs. RHE and an overpotential of -0.660 V vs. RHE (at j = 20 mA/cm^2). The pristine MoS_2 QDs displayed HER onset potential of -0.350 V vs. RHE and an overpotential of -0.455 V vs. RHE (at j = 20 mA/cm^2). The higher HER activity of MoS_2 QDs compared to GNRs is consistent with previous literature.[11] Interestingly, the polarization curves of the C-GNR/MoS_2 heterostructure displayed a well-defined

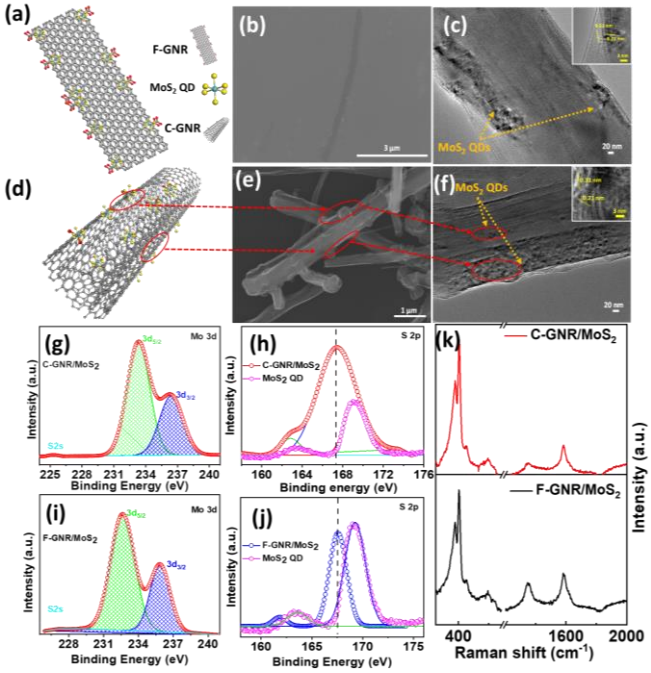

Fig. 1. (a) Schematic of F-GNR/MoS_2 heterostructure (b) SEM image and (c) TEM image of F-GNR/MoS_2. Inset shows the HRTEM image with lattice spacing (d) Schematic of C-GNR/MoS_2 heterostructure (e) SEM image and (f) TEM image of C-GNR/MoS_2. Inset shows the HRTEM image with lattice spacing (g) XPS high resolution spectrum of Mo 3d region in C-GNR/MoS_2 and (h) XPS high resolution spectrum of C-GNR/MoS_2 and pristine MoS_2 QD for S 2p region (i) XPS high resolution spectrum of Mo 3d region in F-GNR/MoS_2 and (h) XPS high resolution spectrum of F-GNR/MoS_2 and pristine MoS_2 QD for S 2p region (k) Raman spectrum of the heterostructures

catalytic wave with two closely placed onsets (Fig. 2a). The initial electrocatalytic onset potential of -0.06 V vs. RHE demonstrated by C-GNR/MoS_2 is one of the best reported from a carbon-based system (very close to Pt onset potential of -0.03 mV vs. RHE) and superior to many metal-based HER catalysts (Table S2†). The second onset in the catalytic wave was observed at -0.145 V vs. RHE. To the best of our knowledge, this is the first study to report an observation of a catalytic wave with dual onsets in GNR/MoS_2 systems, indicating the presence of multiple catalytically active centers. The C-GNR/MoS_2 heterostructure also displayed two Tafel slopes, 68.3 mV/dec and 72.9 mV/dec, corresponding to the first and second onset potentials, respectively (Fig. 2b). From Tafel slope analysis, GNRs and MoS_2 have the Volmer step as the rate-determining step (RDS) whereas, in the vdW heterostructures, a combination of Volmer and Heyrovsky steps govern the process.[14] The lower onset potential and Tafel slope, together with a higher current density, signify the superiority of C-GNR/MoS_2 towards HER. Fig. S11† compares onset and overpotential for attaining 20 $mAcm^{-2}$ for all samples. The analysis of the electrochemically active surface area (ECSA) (Fig. 2c) implied a higher ESCA for C-GNR/MoS_2 heterostructure (illustrated by the higher C_{dl}) compared to F-GNR/MoS_2. The analysis of ECSA for pristine C-GNR and F-GNR is shown in Fig. S12†. Further, the lower charge transfer resistance for the C-GNR/MoS_2 heterostructure, from impedance measurements, suggests faster electron transfer kinetics in the system (Fig. 2d). The C-GNR/ MoS_2 demonstrated excellent stability, with a stable current density up to 12 h (Fig. S13†). No redox process

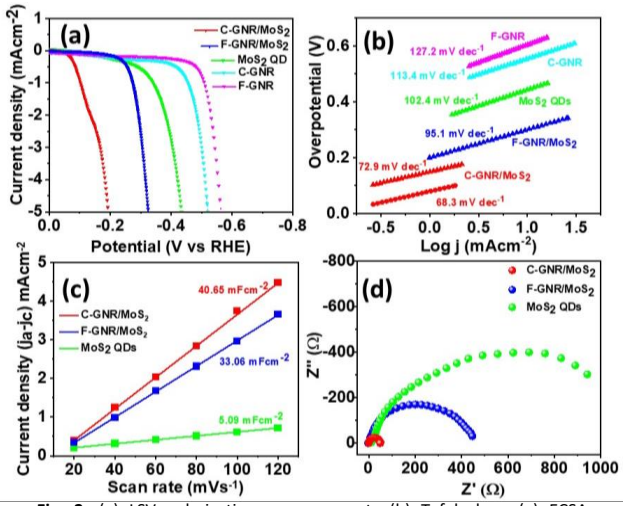

Fig. 2. (a) LSV polarization measurements (b) Tafel slope (c) ECSA measurements (d) EIS measurements

is expected for oxygen functionalities on the GNR edges at the applied potential range as they are reported to be stable in the HER voltage range.[15] Based on our experimental results, we hypothesize that unique strain-dependent electronic charge distribution at the curved basal plane in C-GNRs leads to heterostructure with higher ECSA, dual active sites, and lower charge transfer resistance leading to an excellent HER activity with an ultrasmall onset potential.

We performed DFT-based calculations to verify the hypothesis regarding curvature (strain)-dependent charge redistribution and gain insights into the nature of HER active sites. Fig. S14a† shows the DFT simulated structures of F-GNR and C-GNR. The electron-withdrawing carboxylic acid groups (produced during the unzipping process) at the edges result in the partial polarization of adjacent C=C. The polarization leads to a slightly higher negative charge on the carbon atom adjacent to the carboxylic acid group, increasing the electronic density on the edges (Fig. S14b†). However, in C-GNRs, in addition to the edge sites, the rehybridization of π and σ orbitals at the curved region result in high electron density hotspots towards the center of the curved face, opposite to the unzipped edges. The enhanced electronic density of edge atoms in F-GNR and atoms around the C-GNR curved face, leads to enhanced dipole-dipole interaction with MoS_2 QDs to form the heterostructure and allows effective charge transfer with adsorbed protons for promoting HER (see S.I section 3.1). The lower Gibbs free energy change (ΔG_H) for C-GNRs for the active sites at the center compared to edge sites in C-GNRs and F-GNRs reinforce the experimentally observed higher HER activity (Table S3†). Further, the GNR/MoS_2 heterostructures were optimized in various configurations. (Fig. S15†, Fig. S16†, Fig. S17†). The lowest total energy for the structure confirms the favorable anchoring of QDs near the edges in F-GNR. However, in the case of C-GNR, MoS_2 gets anchored at the edges and towards the curved center (Fig. 3a). Thus, the DFT calculations substantiate the distinctly different distribution of MoS_2 QDs in C-GNR and F-GNR-based heterostructures, as seen in HRTEM images. Moreover, our calculations indicated an increased electron accumulation at the sulfur atom of MoS_2 QDs at the interface in the heterostructure (higher electronic density) (Fig. 3b), potentially due to the electron transport from GNRs to MoS_2 as seen in the XPS and Raman analysis. The DOS calculations also support the electron transfer, which showed that DOS for MoS_2 in the heterostructure is positioned higher than in pristine MoS_2 QDs (Fig. 3c). DFT analysis also suggested that the interfacial sulfur atoms have the lowest ΔG_H among the investigated potential active sites (Table S3†), confirming the interfacial S as the most efficient active site. The presence of MoS_2 at the edges and center of the curved plane in C-GNRs, could potentially have different HER activity and is leading to the catalytic wave with dual onsets (Fig. 2a). The proton adsorption energies for the interfacial S sites at the edge and center in C-GNR/MoS_2 heterostructure were calculated to compare their HER activity. As expected, the DFT analysis showed different proton adsorption energy and ΔG_H for the two interfacial S active sites in C-GNR/MoS_2 heterostructure. The smaller proton adsorption energy (-0.058 eV for center and 0.092 eV for edge) and lower ΔG_H for the interfacial sulfur active sites at the center of the curvature in the C-GNR/MoS_2 (compared to the one at the edge) leads to optimal binding strengths of H atoms and consequent better onset and HER activity (Fig. 3d). Thus, it can be inferred that the first onset in the catalytic wave in the HER polarization curve of C-GNR/MoS_2 is due to the interfacial S atom near the curved plane in C-GNRs, and the second onset comes from the interfacial S active site at the edges. Moreover, the higher number of electronic states close to the Fermi level in C-GNR/MoS_2 indicates high carrier density and improved charge

transfer, which strongly supports the experimental results (Fig. 3e). Hence, our DFT calculations confirm that the variations in local electronic charge distributions play a critical role in determining the activity in GNRs and the interfacial sulfur in MoS_2 are the active sites for C-GNR/MoS_2 heterostructure leading to the catalytic wave.

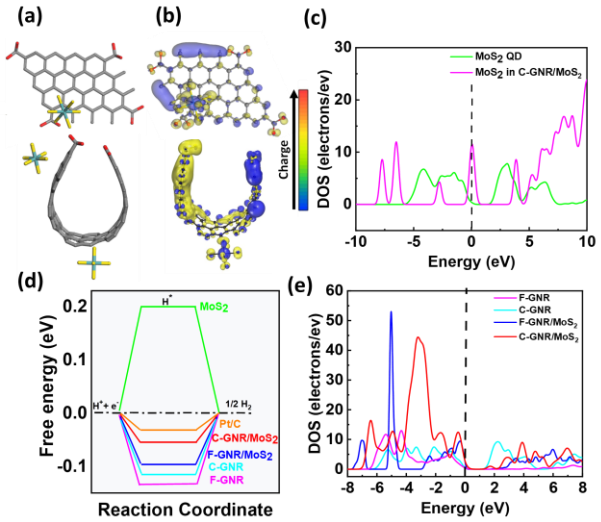

Fig. 3. (a, b) Stick representation and electric field distribution of idealized F-GNR/MoS_2 (top) and C-GNR/MoS_2 (bottom), respectively (c) DOS plot for MoS_2 alone (d) Gibbs free energy diagram (e) Total density of states representation.

In summary, the curvature-induced lattice strain and localized electronic density variations, and specific anchoring of MoS_2 QDs in C-GNR lead to significantly different and improved catalytic activity in GNR-based heterostructures. Due to the electron transfer from GNR to the interfacial S in MoS_2 QDs, the interfacial S atom becomes significantly activated towards HER resulting in superior HER activity of the heterostructure. Unlike F-GNR, the curvature-triggered electron redistribution in C-GNRs led to the anchoring of MoS_2 QDs in C-GNR near the edge and at the center of the curved lattice. The presence of two catalytic sites is demonstrated by a catalytic wave with two closely positioned onsets for HER with the first onset potential as low as -60 mV. Our DFT simulation helped us confirm the identity of the active sites and reinforced the experimental results. The curvature-controlled electron localization in graphenic systems opens avenues to develop novel Pt-group metal-free catalysts with an enhanced and selective catalytic activity that can augment future energy sustainability.

S.T.S. acknowledges the financial support through DOE grant # DE-FE0031908. This work was performed, in part, at the Center for Integrated Nanotechnologies, a User Facility operated for the DOE, Office of Science by Los Alamos National Laboratory (Contract 89233218CNA000001), and Sandia National Laboratories (Contract DE-NA-0003525). S.T.S also acknowledges the partial support from a seed grant through Nanotechnology collaborative Infrastructure (NCI)-Southwest program supported partly by NSF program NNCI-ECCS-15421. We acknowledge the use of the Eyring Materials Center core facilities at Arizona State University, supported in part by NSF award ECCS-2025490.

Conflicts of interest

There are no conflicts to declare

References

1 (a) Y. Zhao, R. Nakamura, K. Kamiya, S. Nakanishi and K. Hashimoto, *Nat. Commun.*, 2013, **4**, 1-7; (b) D. Voiry, H. S. Shin, K. P. Loh and M. Chhowalla, *Nat. Rev. Chem.*, 2018, **2**, 1-17; (c) Y. Zheng, Y. Jiao, Y. Zhu, L. H. Li, Y. Han, Y. Chen, A. Du, M. Jaroniec and S. Z. Qiao, *Nat. Commun.*, 2014, **5**, 1-8; (d) Y. Zheng, Y. Jiao, J. Chen, J. Liu, J. Liang, A. Du, W. Zhang, Z. Zhu, S. C. Smith and M. Jaroniec, *J. Am. Chem. Soc.*, 2011, **133**, 20116-20119.

2 (a) K. Chang and W. Chen, *Chem. Commun.*, 2011, **47**, 4252-4254; (b) L. Tao, Y. Wang, Y. Zou, N. Zhang, Y. Zhang, Y. Wu, Y. Wang, R. Chen and S. Wang, *Adv Energy Mater.*, 2020, **10**, 1901227; (c) R. K. Biroju, D. Das, R. Sharma, S. Pal, L. P. Mawlong, K. Bhorkar, P. Giri, A. K. Singh and T. N. Narayanan, *ACS Energy Lett.*, 2017, **2**, 1355-1361; (d) A. R. Puente Santiago, T. He, O. Eraso, M. A. Ahsan, A. N. Nair, V. S. Chava, T. Zheng, S. Pilla, O. Fernandez-Delgado and A. Du, *J. Am. Chem. Soc.*, 2020, **142**, 17923-17927; (e) Y. Zhu, W. Peng, Y. Li, G. Zhang, F. Zhang and X. Fan, *J. Mater. Chem. A.*, 2019, **7**, 23577-23603.

3 (a) K.C. Pham, Y.H. Chang, D. S. McPhail, C. Mattevi, A. T. Wee and D. H. Chua, *ACS Appl. Mater. Interfaces*, 2016, **8**, 5961-5971; (b) D. H. Youn, S. Han, J. Y. Kim, J. Y. Kim, H. Park, S. H. Choi and J. S. Lee, *ACS nano*, 2014, **8**, 5164-5173; (c) M. H. Lee, D. H. Youn and J. S. Lee, *Appl. Catal. A: Gen.*, 2020, **594**, 117451; (d) Q. Liu, Z. Pu, A. M. Asiri and X. Sun, *Electrochim. Acta*, 2014, **149**, 324-329.

4 (a) R. Wang, Y. Jing, P. Sun and X. Wang, *Mater. Lett.*, 2021, **294**, 129779; (b) W. Gao, Y. Shi, Y. Zhang, L. Zuo, H. Lu, Y. Huang, W. Fan and T. Liu, *ACS Sustain. Chem. Eng.*, 2016, **4**, 6313-6321.

5 N. Mohanty, D. Moore, Z. Xu, T. Sreeprasad, A. Nagaraja, A. A. Rodriguez and V. Berry, *Nat Commun.*, 2012, **3**, 1-8.

6 D. V. Kosynkin, A. L. Higginbotham, A. Sinitskii, J. R. Lomeda, A. Dimiev, B. K. Price and J. M. Tour, *Nature*, 2009, **458**, 872-876.

7 (a) M. López-Sancho and M. Munoz, *Phys. Rev. B*, 2011, **83**, 075406; (b) A. Kleiner and S. Eggert, *Phys. Rev. B*, 2001, **64**, 113402.

8 J. Deng, H. Li, J. Xiao, Y. Tu, D. Deng, H. Yang, H. Tian, J. Li, P. Ren and X. Bao, *Energy Environ. Sci.*, 2015, **8**, 1594-1601.

9 T. Wang, Z. Wang, R. V. Salvatierra, E. McHugh and J. M. Tour, *Carbon*, 2020, **158**, 615-623.

10 S. Shang, L. Gan, C. W. M. Yuen, S.-x. Jiang and N. M. Luo, *Compos. Part A Appl. Sci Manuf.*, 2015, **68**, 149-154.

11 (a) L. Najafi, S. Bellani, B. Martin-Garcia, R. Oropesa-Nunez, A. E. Del Rio Castillo, M. Prato, I. Moreels and F. Bonaccorso, *Chem. Mater.*, 2017, **29**, 5782-5786; (b) Y. Li, H. Wang, L. Xie, Y. Liang, G. Hong and H. Dai, *J. Am. Chem. Soc.*, 2011, **133**, 7296-7299; (c) X. Yu, G. Zhao, S. Gong, C. Liu, C. Wu, P. Lyu, G. Maurin and N. Zhang, *ACS Appl. Mater. Interfaces*, 2020, **12**, 24777-24785.

12 F. Joucken, Y. Tison, P. Le Fèvre, A. Tejeda, A. Taleb-Ibrahimi, E. Conrad, V. Repain, C. Chacon, A. Bellec and Y. Girard, *Sci. Rep.*, 2015, **5**, 1-10.

13 T. Pandey, A. P. Nayak, J. Liu, S. T. Moran, J. S. Kim, L. J. Li, J. F. Lin, D. Akinwande and A. K. Singh, *Small*, 2016, **12**, 4063-4069.

14 (a) A. P. Murthy, J. Theerthagiri and J. Madhavan, *J. Phys Chem. C*, 2018, **122**, 23943-23949; (b) T. Shinagawa, A. T. Garcia-Esparza and K. Takanabe, *Sci. Rep.*, 2015, **5**, 1-21.

15 A. A. Kobets, A. A. Iurchenkova, I. P. Asanov, A. V. Okotrub and E. O. Fedorovskaya, *Phys. Status Solidi B*, 2019, **256**, 1800700.